RSC Advances

ROYAL SOCIETY OF CHEMISTRY

www.rsc.org/advances

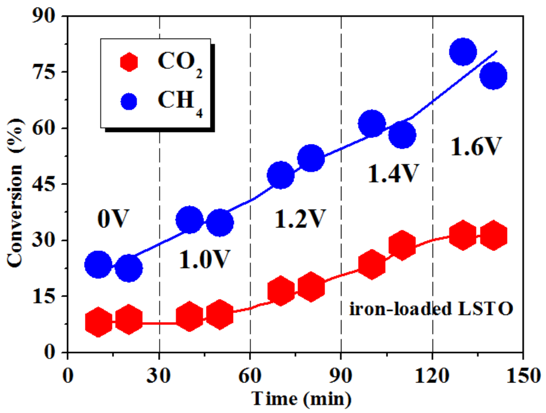

Direct electrochemical biogas reforming is successfully demonstrated in solid oxide electrolyser with titanate cathode under external voltages.

Journal Name RSCPublishing

ARTICLE

Cite this: DOI: 10.1039/x0xx00000x

Received 00th January 2012,
Accepted 00th January 2012

DOI: 10.1039/x0xx00000x

www.rsc.org/

Demonstration of efficient electrochemical biogas reforming in a solid oxide electrolyser with titanate cathode

Qingqing Qin,[a] Kui Xie,[a,b] * Haoshan Wei,[a] Wentao Qi,[a] Jiewu Cui,[a] Yucheng Wu [a,b] *

Biogas reforming is a renewable and promising way to produce syngas. In this work, we demonstrate a novel strategy to directly and electrochemically convert CH_4/CO_2 into H_2/CO. Electrochemical reforming of dry CH_4/CO_2 (1:1) mixture is successfully achieved in a 10-μm-thick titanate cathode with oxygen byproduct generated in anode in an oxide-ion-conducting solid oxide electrolyser under external voltages. In addition, loading iron nanocatalyst in titanate cathode or/and increasing applied voltages has further improved CH_4/CO_2 conversion. The highest methane conversion of approximately 80% is demonstrated for direct electrochemical reforming in cathode in contrast to the low conversion under open circuit condition in oxide-ion-conducting solid oxide electrolyser cathode.

Introduction

Significant efforts are being devoted to hydrocarbon reforming for syngas production because of the natural abundance CH_4/CO_2 and their derived high-value compounds[1-6]. Currently, most biogas reforming is preferentially performed using heterogeneous catalysis on transition metal oxides loaded with metal nanocatalysts at intermediate to low temperatures[7-9]. Normally, this catalytic process requires activation of methane or carbon dioxide through chemical adsorption on surface defect sites or thermal splitting methane on metal catalyst. The stepwise decomposition of CH_4 into CH_x fragments on a metal surface can significantly benefit the catalysis conversion. On the other hand, the chemisorption and dissociation of CO_2 on a transition metal surface is also favorable for efficient dry CO_2 reforming of CH_4. The recycling of CO_2 in this new way would advance us into a carbon-neutral renewable and sustainable energy cycle[10-14].

Solid oxide electrolyser is a high-efficiency energy conversion device to produce clean fuel *via* high-temperature electrolysis with favourable kinetics and thermodynamic[15, 16]. Oxide-ion-conducting solid oxide electrolyser can directly electrolyze carbon dioxide into carbon monoxide and oxygen using external electricity[17-20]. In this process, CO_2 molecules in cathode are firstly split into active CO^- and O^- which are then electrochemically transformed into CO and O^{2-}, respectively. The oxide ion is then simultaneously transported through electrolyte to anode and forms oxygen. We have recently demonstrated the successful electrochemical conversion of CO_2/H_2O into syngas in a solid oxide electrolyser with a configuration $(La_{0.8}Sr_{0.2})_{0.95}MnO_{3-\delta}/YSZ/La_{0.2}Sr_{0.8}TiO_{3+\delta}$[21]. The hydrogen species produced from steam splitting can further react with CO_2 or CO to give rise to synthetic fuels in the presence of appropriate metal catalysts. Therefore, this feature of CO_2 electrolysis makes it possible to *in-situ* utilise the O^- at the three-phase boundary of cathode to efficiently oxidize methane into syngas in the presence of appropriate metal catalysts before it is transformed to O^{2-} and transported to anode under sufficient external loads. The thermal splitting of CH_4 into CH_x fragments on thin electrode surface also benefits the catalytic oxidation process.

The conventional Ni/YSZ electrode has exhibited excellent high-temperature electrolysis performance under a reducing atmosphere; however, the Ni-cermets are not redox-stable and require a high concentration of reducing gas flowing over the Ni metal to avoid the oxidation of Ni to NiO[22, 23]. We have also found that the mixture of CO_2/H_2O can quickly oxidize Ni metal to amorphous phase composed of NiO and $Ni(OH)_2$, which leads to rapid cathode performance degradations[24]. Furthermore, the catalytic activity of Ni metal towards CO_2 splitting is relatively high; carbon deposition most likely occurs and results in cell performance degradation. Some researchers have demonstrated that the carbon deposition is likely caused by reactions that occur over the catalyst and favour to occur only when CO is present in the chemical reaction system[25-28]. In contrast to Ni-YSZ, perovskite-type $La_xSr_{1-x}TiO_{3+\delta}$ (LSTO) is an active and redox-stable material with high n-type conductivity upon reduction, which has attracted a great deal of attention in the field of electrode material for solid oxide electrolysers[29-31]. The n-type conductivity of ~100 $S\cdot cm^{-1}$ has been demonstrated if the LSTO is strongly reduced[32]. The n-type conduction mechanism would well fit the strong reducing condition in cathode and provide excellent electrode performances.

The direct and efficient CH_4 oxidation is demonstrated in a solid oxide fuel cell with titanate anode[33]. Hirata *et al.* conducted electrochemical reforming of CH_4 with CO_2 in porous cells with Cu in the anode and achieved stable formation of H_2 and CO fuel[34]. R. J. Kee *et al*. reported the experimental and modeling investigations of thermal methane reforming chemistry within porous Ni-YSZ anode of solid oxide fuel cell[35]. The electrochemical reaction could directly promote the reforming or conversion of methane at the anode side, which requires an anode material that has good catalytic reforming and electrochemical reactivity[36].

In this study, we demonstrate *in situ* electrochemical biogas reforming in an oxide-ion-conducting solid oxide electrolyser with titanate cathode. Electrochemical catalysis process is studied *versus* applied voltage from 0 to 1.6 V. Active iron nanoparticles are loaded to titanate cathode to further improve biogas reforming performances.

Experimental

All the powders used in this current investigation were of analytical grade and purchased from SINOPHARM Chemical Reagent Co.Ltd (China) unless specified otherwise. The $La_{0.2}Sr_{0.8}TiO_{3+\delta}$ (LSTO) powders were synthesized by a combustion method[37]. The collected product was fired at 1300 ^oC with a heating and cooling rate of 5 $°C\cdot min^{-1}$ up to 6 h in air. The $(La_{0.8}Sr_{0.2})_{0.95}MnO_{3+\delta}$ (LSM) powders were prepared by solid-state reaction method as described elsewhere[38] with the final heat treatment temperature at 1100 ^oC (3 $^oC\cdot min^{-1}$) for 3 h in air. A combustion method was employed for $Ce_{0.8}Sm_{0.2}O_{2-\delta}$ (SDC) powders synthesis using Sm_2O_3 and $Ce(NO_3)_4\cdot 6H_2O$ followed by a heat treatment at 800 ^oC (3 $^oC\cdot min^{-1}$) for 3 h in air. The phase formations of the above prepared powders were analyzed and identified by X-ray diffraction (XRD, CuKα, $2\theta = 3^o\cdot min^{-1}$, D/MAX2500V, Rigaku Cooperation, Japan) with 2θ ranging from 10 to 80°. High-resolution transmission electron microscopy (HRTEM, JEM-2100F, JEOL Ltd, Japan) with selected area diffraction operating at 200 kV was performed to observe the oxidized and reduced LSTO powders. The valence states of elements in the oxidized and reduced samples were determined using X-Ray Photoelectron Spectroscopy (XPS) on a Thermo ESCALAB 250 with Al-Kα (1486.6 eV) radiation source. The binding energies were calibrated to the C_{1s} peak at 285 eV.

About 2.0 g of LSTO powders were pressed into bars at a pressure of 6 MPa and then sintered at 1400 °C (3 °C·min^{-1}) for 5 h in air to obtain samples for conductivity tests. The bar with relative density of approximately 85% was reduced at 1400 °C (3 °C·min^{-1}) for 10 h in 5%H_2/Ar (99.99% in purity) at a flow rate of 32 ml·min^{-1}. The conductivity was tested in 5%H_2/Ar using a DC four-terminal method from room temperature to 800 °C with the conductivity recorded at a temperature step of 0.5 °C using an online multi-meter (Keithley 2000, Keithley Instruments Inc., USA) [39]. The pO_2 was simultaneously recorded using an online oxygen sensor (Type 1231, ZrO_2-based oxygen sensor, Noveltech, Australia) at 800 °C. The air flow was controlled at 0.5 ml·min^{-1} to change pO_2 at 800 °C. A group of 2-mm-thick YSZ supports were prepared by dry-pressing YSZ powders at the pressure of 8 MPa with a diameter of 20 mm and thickness of 3 mm and then sintered at 1550 °C (3 °C·min^{-1}) for 20 h in air. The prepared LSTO and SDC powders were mixed in alpha-terpineol at a 65:35 weight ratio with appropriate amounts of cellulose additive (approximately 10% weight ratio in contrast to the ceramic powders) to form electrode slurry. The YSZ disc surfaces were then coated with the slurry in an area of 1.0 cm^2 and then treated at 1000 °C (3 °C·min^{-1}) for 3 h in air to assemble symmetrical cells. The electrode based on LSTO-SDC loaded with 2 wt% iron oxide was prepared by infiltrating the required amount of nitrate followed by a heat treatment at 550 °C (5 °C·min^{-1}) for 30 min in air. In order to determine the particle size, the impregnation solution is dried and then treated at different temperatures from 400-800 °C respectively. Then XRD is used to test the iron oxide powders and the particle size is calculated according to Scherrer equation[40-43]. The size of iron oxide in cathode is around 25 nm; however, it grows to 55 nm at the operation temperature of 800 °C as shown in Fig.S11. The current collection layer was constructed by printing silver paste (SS-8060, Xinluyi, Shanghai, China) on both electrode surfaces. An external circuit was performed with silver wire (0.4 mm in diameter), which was connected to current collectors using conductive adhesive (DAD87, Shanghai Research Institute for Synthetic Resins, Shanghai, China) followed by a heat treatment at 550 °C (3 °C·min^{-1}) for 30 min in air. Single solid oxide electrolyser with LSM-SDC anode was prepared in the same way as discussed above. The electrode microstructures were investigated by Scanning Electron Microscopy (SEM, JSM-6490LV, JEOL Ltd, Japan) coupled with Energy Dispersive Spectroscopy (EDS).

The symmetrical cell was tested under different hydrogen or methane partial pressure at 800 °C using an electrochemical station (IM6, Zahner, Germany) with a frequency range of 4 M-0.1 Hz in a two-electrode mode, respectively. The electrode polarization resistance was calculated by modeling the spectra using Zview software[38]. The hydrogen partial pressure and methane partial pressure were changed by adjusting the gas flow rates of H_2 (99.99%), CH_4 (99.99%) and Ar(99.999%) using a mass flow meter (D08-3F, Sevenstar, China) while the total flow rate was controlled at 20 ml·min^{-1}. Then, single solid oxide electrolyser with LSTO-SDC and iron-loaded LSTO-SDC cathodes were investigated for biogas reforming, respectively. The solid oxide electrolysers were sealed to a home-made testing jig by using ceramic paste (JD-767, Jiudian, Dongguan, China) for electrochemical measurements. The AC impedance spectroscopy and current-*versus*-voltage curve (I-V curve) of the electrolysers were recorded at a step of 0.004 V·s^{-1}. The mixed gas of 20%CH_4/20%CO_2/60%Ar was supplied to cathode while the anode was exposed to static air. The gas flow rate was controlled at 20 ml·min^{-1} using mass flow meters. The output gas from cathode was analyzed using an online gas chromatograph (GC9790II, Fuli, Zhejiang, China) to detect the concentration of generated hydrogen and carbon monoxide.

Results and discussion

The XRD Rietveld refinement patterns of the LSTO and iron oxide-loaded LSTO are shown in Figs.1 (a1) and (b1), respectively. Accordingly, Figs.1 (a2) and (b2) represent the reduced samples treated in 5%H_2/Ar for 3 h at 800 °C, respectively. The experimental and calculated results indicate that the phase structure of both oxidized and reduced LSTO samples are in *Pm-3m* space group[44]. As shown in the figures, the crystal cell volume is 59.794 Å^3 for the oxidized LSTO which is slightly smaller than that of the reduced sample (59.845 Å^3). This is probably due to that titanium is predominant in Ti^{4+} for the oxidized LSTO, whereas there is a part of Ti^{4+} (0.605 Å^3) reduced to Ti^{3+} (0.670 Å^3), which might give rise to the cell volume expansion. HR-TEM analysis of the oxidized and reduced LSTO reveals lattice spacing of 0.274 nm (110) and 0.291 nm (110), respectively, as shown in Figs.2 (a) and (b). The increased lattice spacing of reduced LSTO firmly confirms lattice expansion for the reduced sample as determined by the XRD analysis. Fig.1 (b1) shows the XRD pattern of LSTO loaded with iron oxide, which confirms the presence of α-type iron oxide in cathode. Fig.1 (b2) reveals a sharp diffraction peak ($2\theta=\sim44.6°$) of iron crystal plane (110) for the impregnated LSTO after reduction in a reducing atmosphere, which implies that the iron oxide is transformed into metallic iron metal in 5%H_2/Ar at 800 ºC.

XPS analysis is carried out to establish the chemical states of the oxidized and reduced samples. All spectroscopies are fitted with a Shirley-type background subtraction method[45]. The background-function for different spectroscopy of elements is fitted by 80% Gaussian and 20% Lorenzial peaks. As shown in Fig. 3 (a), only Ti^{4+} is observed in the oxidized LSTO sample; however, a part of the Ti^{4+} is chemically reduced to Ti^{3+} by treating the LSTO sample in a reducing atmosphere. The reduction of Ti^{4+} to Ti^{3+} offers free electron as charge carrier that is expected to significantly contribute to electronic conductivity of the reduced ceramic. Similar change in chemical state of Ti is also observed in LSTO loaded with iron oxide before and after reduction as shown in Figs.3 (b1) and (b2). The Fe2p core level XPS spectra are shown in the Figs. 3 (c1) and (c2). As shown in Fig.3 (c1), the Fe^{3+} (2p1/2) and Fe^{3+} (2p3/2) peaks are observed at 724.31 and 710.90 eV[46, 47], respectively. As shown in Fig. 3 (c2), the Fe^{3+} (2p3/2) peak is observed at 711.46 eV and Fe^{3+} (2p1/2) is at 724.31 eV, with Fe (2p3/2) occurring at 710.43 eV[46, 47]. This further confirms that the iron metal appears after reduction. The iron metal nanocatalyst is expected to contribute to the improved electrode performance.

Reduced LSTO samples are a typical n-type electronic conductor with electronic conductivity as high as 10-100 Scm^{-1} in a reducing atmospheres at intermediate temperatures. Figs.S2 (a) and (b) show that the reduced sample displays typical metallic behaviours with negative temperature coefficients in a 5%H_2/Ar atmosphere. Fig.4 shows the mixed conductivities of the porous LSTO electrode with/without impregnated iron oxide supported on YSZ disks in redox-cycling atmospheres. Two obvious steps are observed in each figure which is identified as the exposure to different atmospheres. The conductivity pulse appears after flowing 5%H_2/Ar over the electrode to expose the porous electrode in a strong reducing atmosphere. The atmosphere with low oxygen partial pressure leads to the conductivity increase because of the transition of Ti^{4+} to Ti^{3+}. It is observed that the conductivities of the porous LSTO electrode are shifting between approximately 0.70 to 1.10 S·cm^{-1} and 0.68 to 1.07 S·cm^{-1} in the redox cycling atmospheres at 800 °C, which further validates the superior redox stability of the LSTO electrode material. In comparison, similar conductivity change has also been observed for the iron oxide loaded LSTO electrode between 0.58 to 1.54 S·cm^{-1} and 0.52 to 1.48 S·cm^{-1} in the redox cycling atmospheres. The loading of iron oxide into the porous LSTO electrode has clearly improved the conductivity, which is accordingly enhanced by 40% in the reducing atmosphere because of the presence of iron metal in the electrode. The iron nanoparticles are expected to strongly increase the catalytic activity in electrochemical biogas reforming process. The different loading contents of iron catalyst in electrode have been studied by several researchers[48-50]. It is suggested that metal catalyst agglomeration occurs with higher loading contents (wt%>4%) and causes electrode performance degradation[51, 52]. Normally, the loading content of 0.5-3.5 wt% offers the optimum electrode performances[53-55].

Fig.5 shows the AC impedance of the symmetric cells tested under a series of hydrogen partial pressure (10, 20, 40, 60, 80 and 100%H_2) at 800 °C. The series resistant of the cell (R_s) corresponds to the first intercept and the difference between the two intercepts is a measure of the electrode polarization resistance (R_p). The Zview software is employed to calculate R_s and R_p values as reported in our previous work[56]. The ionic resistance of YSZ electrolyte mainly contributes to the R_s, which is generally stable in a wide range of hydrogen partial pressure. However, the R_p of the symmetric cell based on LSTO decreased from about 14.74 to 2.19 $\Omega\cdot cm^2$ with the hydrogen partial pressure ranging from 10 to 100% as shown in Figs.5 (a1) and (a2), suggesting that the stronger reducing atmosphere is beneficial to improving the electrode polarizations. In contrast, the R_p of the symmetric cell based on LSTO-SDC with iron nanoparticles significantly decreases with the increasing hydrogen concentration from 4.41 to 1.47 $\Omega\cdot cm^2$, which is probably due to the enhanced electro-catalytic activity under strong reducing atmosphere in the presence of iron nanoparticles. In this case, stronger reducing atmosphere favorers the presence of metallic iron on LSTO electrode surface and thus promotes the electro-catalytic activity. On the other hand, a low oxygen partial pressure is also favourable to increasing electrical conductivity of the reduced LSTO that further improves electrode performances. Similar electrode polarizations have also been observed for the symmetric cells in different methane atmospheres. Figs.6 (b1) and (b2) show the AC impedance of symmetric cells tested at a series of methane partial pressures (5, 20 and 40%CH_4) at 800 °C. The R_p values decrease with increasing methane concentration; however, they are still larger than the polarization values in hydrogen as shown in Figs.6 (a1) and (a2). This is because of that the reducing atmosphere of methane is not comparable to hydrogen and is not sufficient to reduce cathode. In contrast, the R_p based on LSTO with loaded iron nanoparticles significantly decreases with increasing methane concentrations. Therefore, it can be concluded that the iron electro-catalyst significantly enhances the electro-catalytic activity of the composite electrode and hence improves the electrode polarizations.

Fig. 7 presents the microstructures of electrolyte-supported half cells with LSTO and iron-loaded LSTO electrodes, respectively. It can be found that the LSTO and iron-loaded LSTO electrodes are porous and adhere well to the dense YSZ electrolyte. The electrochemical biogas reforming is then investigated in two kinds of solid oxide electrolysers with LSTO and iron loaded-LSTO cathodes under a series of applied voltages ranging from 0 to 1.6 V at 800 °C, respectively. Fig. 8 (a) shows the typical curves of the voltage *versus* current density (V-I curves) of the electrolysers for the electrochemical reforming of dry CH_4/CO_2 mixtures. The maximum current density reaches 145 $mA\cdot cm^{-2}$ at 1.6 V based on LSTO cathode at 800 °C. In contrast, the cell based on iron-loaded LSTO cathode is greatly improved and the current density finally reaches 215 $mA\cdot cm^{-2}$ under the same conditions. As shown in Fig.8 (b), the current densities increase with applied voltages and they are quite stable at a fixed applied potential indicating a stable electrochemical process. The current density with iron-loaded LSTO cathodes reaches 200 $mA\cdot cm^{-2}$ at 1.6 V, which is higher than 120 $mA\cdot cm^{-2}$ for the bare LSTO electrode. Both trends further confirm that the loading of iron catalyst can improve electrode performances, and are therefore expected to increase syngas production *via* electrochemical biogas reforming. Electrocatalytic reforming of carbon dioxide by methane in SOFC system was studied by D. J. Moon *et al.*, who found that reaction of CO_2 and CH_4 under the closed-circuit condition were more stable than those of the open-circuit[57]. In our work, quite stable current densities are also obtained to direct electrochemical reforming of methane with carbon dioxide in oxide-ion-conducting solid oxide electrolyser cathode.

Fig. 9 shows the *in-situ* AC impedance spectroscopy of cells with LSTO and iron-loaded LSTO cathodes under a series of applied voltages ranging from 0 to 1.6 V at 800 °C in $20\%CH_4/20\%CO_2/60\%Ar$, respectively. As shown in the figures, R_s values are stabilized at approximately 1.5 $\Omega\cdot cm^2$, whereas R_p considerably decreases as applied voltage increasing from 0 to 1.6 V. Increasing the voltage is expected to activate the electrodes to the extent that R_p will remarkably decrease as well as improve the kinetic process of the electrode with accompanying improvement in electrode polarizations. The applied voltage gradually and electrochemically reduces the composite cathode, which improves the mixed conductivity and hence enhances the electrocatalytic activity of the composite electrode. Two semicircles are observed in the impedance spectra: the high-frequency arcs (R_1) and low-frequency arcs (R_2). At high-frequency, R_1 of the solid oxide electrolysers with cathodes is stabilized approximately at 0.5 $\Omega\cdot cm^2$ or improving in a narrow range in a wide voltage range. At low frequency, the mass transfer, R_2, dominates the process, which is probably due to the gas conversion, dissociative adsorption and species transfer at TPB. The R_2 remarkably improves from 2.94 to 1.21 $\Omega\cdot cm^2$ for the cell based on the LSTO cathode with the applied voltage ranging from 1.0 to 1.6 V, suggesting the improved kinetics of gas conversion at high voltages. In contrast, the R_2 is significantly reduced to 1.34 $\Omega\cdot cm^2$ at low voltages and further enhanced to 0.75 $\Omega\cdot cm^2$ at high voltages for the cell based on iron-loaded LSTO cathode. Here it may be supposed that the metallic nanoparticles significantly improve the electrocatalytic activity of the composite cathodes, and the passing current further activates the composite electrodes and improves the electrode polarization.

Fig. 10 shows the short-term performance of electrochemical biogas reforming in solid oxide electrolysers based on LSTO and iron-loaded LSTO cathodes, respectively. As shown in Fig. 10 (a), the conversion of CO_2 and CH_4 are 7% and 22% for LSTO cathode under open circuit at 800 °C. Meanwhile, the conversion of CO_2 and CH_4 reach 10% and 25% for the cell based on the iron-loaded LSTO cathode without applied voltage. The conversion dfference between CO_2 and CH_4 is also observed for the repeated experiments in Fig. S8. The reforming of CH_4 with CO_2 is a dominant reaction at 800 °C; however, the simultaneous occurrence of reverse water gas shift would change the carbon oxide conversion ($CO_2+H_2\leftrightarrow CO + H_2O$) [58, 59]. In the meantime, the thermal splitting of CH_4 probably occurs and produces C ($CH_4\rightarrow C+2H_2$) while Boudouard reaction probably takes places ($2CO\leftrightarrow C(s)+CO_2$) [60, 61]. This is expected to further change the conversion of methane and carbon dioxide. However, Sabatier reaction may be negligible because of the high operation temperatures ($CO_2+4H_2\leftrightarrow CH_4+2H_2O$; $CO+3H_2\leftrightarrow CH_4+H_2O$) [62, 63]. It is observed that the conversion of CO_2 and CH_4 increase with the applied voltages, indicating that high voltage remarkably facilitates the electrochemical process in cathodes. The conversion of CO_2 and CH_4 are 25% and 35% through the *in-situ* electrochemical reforming in a 10-μm-thick LSTO cathode at 1.6 V at 800 °C, which is larger than the values without applied voltages as shown in Fig. 10 (a). In addition, the conversion is remarkably enhanced by loading iron catalysts in LSTO cathode. As shown in Fig. 10 (b), the remarkable conversion of CO_2 (32%) and CH_4 (78%) are demonstrated through improving cathode activity by loading catalyst-active iron nanoparticles. The presence of iron catalyst is expected to thermally split CH_4 into CH_x fragments and therefore favors the *in-situ* biogas reforming in thin-layer cathode.

Fig. 11 shows the production of CO and H_2 from biogas reforming in the cell based with LSTO and iron-loaded LSTO cathodes under a series of applied voltages ranging from 0 to 1.6 V at 800 °C, respectively. The iron nanoparticles can significantly improve electrocatalytic activity. It is found that composite electrode loaded with iron catalyst demonstrates remarkably high performance for steam electrolysis or carbon dioxide electrolysis at applied voltages[50, 64-66]. On the other hand, applied voltage can electrochemically activate electrode as reported by several researchers[67, 68]. For this reason, the iron-loaded LSTO demonstrates a superior behavior even under close circuit conditions in contrast the bare electrodes. At applied voltages, efficient dry reforming of CH_4/CO_2 mixtures is therefore achieved. The yields of CO and H_2 accordingly increase when applied potential increases from 0 to 1.6 V. Higher applied potentials produce stronger reducing conditions in cathode and further activate the electrode for electrochemical splitting of CO_2 to oxide radicals that is therefore beneficial to the *in-situ* oxidation of hydrocarbons. As shown in Fig. 11 (a), H_2 is produced at the rate of 3.17×10^{-3} $mol\cdot s^{-1}$ with bare LSTO at 1.6 V, whereas the H_2 yield reaches approximately 5.64×10^{-3} $mol\cdot s^{-1}$ based on iron-loaded LSTO cathode. The CO is produced at the rate of 3.37×10^{-3} and 5.97×10^{-3} $mol\cdot s^{-1}$ at 1.6 V for the cells with LSTO and iron-loaded LSTO cathodes as shown in Fig. 11 (b), respectively. Both of the trends further confirm that loading iron catalyst is able to significantly improve cathode performances and hence the production of CO and H_2. However, it should be noted that only tiny amount of steam is detected at low voltages and the steam is even absent at higher voltages. The steam is a product of biogas reforming but further split to oxidize methane or produce hydrogen in cathode.

Dry CO_2 reforming of methane is an extremely endothermic reaction [$CH_4+CO_2 \rightarrow 2CO+2H_2$][69, 70], which shows that CO_2 reforming of methane produces a syngas with a H_2/CO ratio close to 1:1. There simultaneously occur water gas shift reaction [$CO_2+H_2\leftrightarrow CO+H_2O$] [58, 59], CH_4 decomposition [$CH_4\rightarrow C(s) +2H_2$] [60], Boudouard reaction [$2CO \rightarrow C(s)+CO_2$] [61] and Sabatier reaction [$CO_2+4H_2\leftrightarrow CH_4+2H_2O$, $CO+3H_2\leftrightarrow CH_4+H_2O$] [62, 63]. And these side reactions sometimes influence final conversion of methane and carbon dioxide. Electrochemical biogas reforming not only utilizes the above reactions but also use the applied voltages to achieve *in-situ* electrochemical reforming in cathode. The carbon dioxide can be electrochemically split into oxide ion and carbon monoxide in cathode. Then part of the oxide ion can be *in-situ* utilized to electrochemically oxide methane and generate syngas [$CO_2+2e^-\rightarrow CO+O^{2-}$, $CH_4+O^{2-}\rightarrow CO+2H_2+2e^-$]. This electrochemical process in cathode is expected to significantly enhance the conversion of carbon dioxide and methane and therefore offers a novel promising alternative for carbon dioxide reforming of methane.

Conclusions

In this work, direct electrochemical biogas reforming is demonstrated in an oxide-ion-conducting solid oxide electrolyser with titanate cathode. Efficient dry reforming of CH_4/CO_2 mixtures is successfully achieved in a thin-layer cathode under external electrical voltages. High conversion of CO_2 (32%) and CH_4 (78%) are obtained through *in-situ* electrochemical reforming in cathode. The presence of catalytic-active iron nanoparticles leads to enhanced CO_2/CH_4 conversion and CO/H_2 production from the *in-situ* electrochemical biogas reforming. The present results offer an alternative way to efficiently convert hydrocarbons into syngas.

Acknowledgement

This work was financially supported by the Natural Science Foundation of China (NSFC), No. 21303037, the China Postdoctoral

Science Foundation, No. 2013M53150, the Ministry of Education of Overseas Returnees Fund, No. 20131792, and the Fundamental Research Funds for the Central Universities, No. 2012HGZY0001.

Notes and references

[a] Department of Energy Materials, School of Materials Science and Engineering, Hefei University of Technology, No.193 Tunxi Road, Hefei, Anhui 230009, China.
[b] Key Laboratory of Advanced Functional Materials and Devices, Hefei University of Technology, No.193 Tunxi Road, Hefei, Anhui 230009, China.
*Corresponding: xiekui@hfut.edu.cn

† Footnotes should appear here. These might include comments relevant to but not central to the matter under discussion, limited experimental and spectral data, and crystallographic data.
Electronic Supplementary Information (ESI) available: [details of any supplementary information available should be included here]. See DOI: 10.1039/b000000x/

1 X. S. Wu and S. Kawi, *Energy Environ. Sci.*, 2010, **3**, 334-342.

2 P. Tang, Q. J. Zhu, Z. X. Wu and D. Ma, *Energy Environ. Sci.*, 2014.

3 T. Shishido, M. Sukenobu, H. Morioka, R. Furukawa, H. Shirahase and K. Takehira, *Catal. Lett.*, 2001, **73**, 21-26.

4 E. B. Pereira, P. Ramı´rez de la Piscina, S. Martı´ and N. Homs, *Energy Environ. Sci.*, 2010, **3**, 487-493.

5 E. Perry Murray, T. Tsai and S. A. Barnett, *Nature*, 1999, **400**, 649-651.

6 C. H. Yang, Z. B. Yang, C. Jin, G. L. Xiao, F. L. Chen and M. F. Han, *Adv. Mater.*, 2012, **24**, 1439-1443.

7 C. Jin, C. H. Yang, F. Zhao, A. Coffin and F. L. Chen, *Electrochem. Commun.*, 2010, **12**, 1450-1452.

8 K. Tomishige, O. Yamazaki, Y. G. Chen, K. Yokoyama, X. H. Li and K. Fujimoto, *Catal. Today*, 1998, **45**, 35-39.

9 J. Wei and E. Iglesia, *J. Catal.*, 2004, **224**, 370-383.

10 M. C. J. Bradford and M. A. Vannice, *Catal. Rev. -Sci. Eng.*, 1999, **41**, 1-42.

11 G. Kim, G. Corre, J. T. S. Irvine, J. M. Vohs and R. J. Gorte, *Electrochem. Solid-State Lett.*, 2008, **11**, B16-B19.

12 J. Sfeir, P. A. Buffat, P. M¨ockli, N. Xanthopoulos, R. Vasquez, H. J. Mathieu, J. V. Herle and K. R. Thampi, *J. Catal.*, 2001, **202**, 229-244.

13 R. J. Gorte, H. Kim and J. M. Vohs, *J. Power Sources*, 2002, **106**, 10-15.

14 N. Laosiripojana and S. Assabumrungrat, *J. Power Sources*, 2007, **163**, 943-951.

15 G. Tsekouras, D.Neagu and J. T. S. Irvine, *Energy Environ. Sci.*, 2013, **6**, 256-266.

16 M. Ni, M. K. H. Leung and D. Y. C. Leung, *Int. J. Hydrogen Energy,* 2008, **33**, 2337-2354.

17 K. Xie, Y. Q. Zhang, G. Y. Meng and J. T. S. Irvine, *J. Mater. Chem.*, 2011, **21**, 195-198.

18 W. T. Qi, Y. Gan, D. Yin, Z. Y. Li, G. J. Wu, K. Xie and Y. C. Wu, *J. Mater. Chem. A*, 2014, **2**, 6904-6915.

19 K. R. Sridhar and B. T. Vaniman, *Solid State Ionics*, 1997, **93**, 321-328.

20 Y. X. Li, Y. Gan, S. S. Li, Y. Wang, H. F. Xiang and K. Xie, *Phys. Chem. Chem. Phys.*, 2012, **14**, 15547-15553.

21 K. Xie, Y. Q. Zhang, G. Y. Meng and J. T. S. Irvine, *Energy Environ. Sci.*, 2011, **4**, 2218-2222.

22 D. Neagu, J. T. S. Irvine, *Chem. Mater.*, 2010, **22**, 5042-5053.

23 A. Ghosh, A. K. Azad and J. T. S. Irvine, *ECS Transactions*, 2011, **35**, 1337-1343.

24 G. J. Wu, K. Xie, Y. C. Wu, W. T. Yao and J. Zhou, *J. Power Sources*, 2013, **232**, 187-192.

25 S. D. Ebbesen and M. Mogensen, *J. Power Sources*, 2009, **193**, 349-358.

26 X. C. Lu, J. - H. Zhu, *Solid State Ionics*, 2007, **178**, 1467-1475.

27 D. Neagu, G. Tsekouras, D. N. Miller, H. Me´nard and J. T. S. Irvine, *Nat. Chem.*, 2013, **5**, 916-923.

28 X. D. Yang , J. T. S. Irvine, *J. Mater. Chem.*, 2008, **18**, 2349-2354.

29 A. D. Aljaberi, J. T. S. Irvine, *J. Mater. Chem. A*, 2013, **19**, 5868-5874.

30 X. Li, H. L. Zhao, X. Zhou, N. S. Xu, X. Zhou, C. J. Zhang and N. Chen, *Int. J. Hydrogen Energy*, 2009, **34**, 6407-6414.

31 D. N. Miller, J. T. S. Irvine, *J. Power Sources*, 2011, **196**, 7323-7327.

32 Y. Gan，Q. Q. Qin, S. G. Chen，Y. Wang, D. H. Dong, K. Xie and Y. C. Wu, *J. Power Sources*, 2014, **245**, 245-255.

33 J. C. Ruiz-Morales, J. Canales-Va´zquez, C. Savaniu, D. MarreroLo´pez, W. Zhou and J. T. S. Irvine, *Nature*, 2006, **439**, 568-671.

34 Y. Suga, R. Yoshinaga, N. Matsunaga, Y. Hirata and S. Sameshima, *Ceram. Int.*, 2012, **38**, 6713-6721.

35 E. S. Hecht, G. K. Gupta, H. Y. Zhu, A. M. Dean, R. J. Kee, L. Maier and O. Deutschmann, *Appl. Catal A: General*, 2005, **295**, 40-51.

36 S. Matayoshi, Y. Hirata, S. Sameshima, N. Matsunaga and Y. Terasawa, *J. Ceram. Soc. Japan*, 2009, **117**, 1147-1152.

37 S. S. Xu, D. H. Dong, Y. Wang, W. Doherty, K. Xie and Y. C. Wu, *J. Power Sources*, 2014, **246**, 346-355.

38 S. S. Li, Y. X. Li, Y. Gan, K. Xie and G. Y. Meng, *J. Power Sources*, 2012, **218**, 244- 249.

39 M. Vracar, A. Kuzmin, R. Merkle, J. Purans, E. A. Kotomin, J. Maier and O. Mathon, *Phys. Rev. B*, 2007, **6**, 174107.

40 A. Monshi, M. R. Foroughi and M. R. Monshi, *World J. Nanosci. Eng.*, 2012, **2**, 154-160.

41 C. Solliard, *Surf. Sci.*, 1981, **106**, 58-63.

42 J. Langford and A. Wilson, *J. Appl. Cryst.*, 1978, **11**, 102-103.

43 A. W. Burton, K. Ong, T. Rea, I. Y. Chan, *Micropor. Mesopor. Mat.*, 2009, **117**, 75-90.

44 J. Canales-Va´zquez, S. W. Tao and J. T. S. Irvine, *Solid State Ionics*, 2003, **159**, 159-165.

45 Y. X. Li, Y. Wang, W. Doherty, K. Xie and Y. C. Wu, *ACS Appl. Mater. Interfaces*, 2013, **5**, 8553-8562.

46 M. Vracar, A. Kuzmin, R. Merkle, J. Purans, E. A. Kotomin, J. Maier and O. Mathon, *Phys. Rev. B*, 2007, **76**, 174107.

47 P. Jiang, L. Bi, X. Y. Sun, D. H. Kim, D. Jiang, G. H. Wu, G. F. Dionne and C. A. Ross, *Inorg. Chem.*, 2012, **51**, 13245-13253.

48 X. Y. Xu, C. R. Xia, G. L. Xiao and D. K. Peng, *Solid State Ionics*, 2005, **176**, 1513-1520.

49 C. J. Fu, Q. L. Liu, S. H. Chan, X. M. Ge and G. Pasciak, *Int. J. Hydrogen Energy*, 2010, **35**, 11200-11207.

50 C. Ruan, K. Xie, L. M.Yang, B. Ding and Y. C. Wu, *Int. J. Hydrogen Energy*, 2014, **39**, 10338-10348.

51 Y. X. Li, G. J. Wu, C. Ruan, Q. Zhou, Y. Wang, W. Doherty, K. Xie and Y.C. Wu, *J. Power Sources*, 2014, *253*, 349-359.

52 M. Lomberg, E. Ruiz-Trejo, G. Offer and N. P. Brandon, *J. Electrochem. Soc.*, 2014, **161**, F899-F905.

53 P. Kim-Lohsoontorn, Y.-M. Kim, N. Laosiripojana and J. Bae, *Int. J. Hydrogen Energy*, 2011, **36**, 9420-9427.

54 Z. B. Liu, B. B. Liu, D. Ding, Z.Y. Jiang and C. R. Xia, *Int. J. Hydrogen Energy*, 2012, **37**, 4401-4405.

55 C. D. Savaniu, J. T. S. Irvine, *Solid State Ionics*, 2011,**192**, 491-493.

56 Y. X. Li, Y. Gan, Y. Wang, K. Xie and Y. C. Wu, *Int. J. Hydrogen Energy*, 2013, **38**, 10196-10207.

57 D. J. Moon, J. W. Ryu, *Cata. Today*, 2003, **87**, 255-264.

58 M. Wisniewski, A. Bore´ave and P. Ge´lin, *Catal. Commun.*, 2005, **6**, 596-600.

59 H. Timmermann, D. Fouquet, A. Weber, E. Ivers-Tiffée, U. Hennings and R. Reimert, *Fuel Cells*, 2006, **6**, 307-313.

60 M. Ando, Y. Hirata, S. Sameshima and N. Matsunaga, *J. Ceram. Soc. Japan*, 2011, **119**, 794-800.

61 S. Assabumrungrat, N. Laosiripojana and P. Piroonlerkgul, *J. Power Sources*, 2006, **159**, 1274-1282.

62 S. K. Hoekman, A. Broch, C. Robbins and R. Purcell, *Int. J. Greenh. Gas Con.*, 2010, **4**, 44-50.

63 K. R. Thampi, J. Kiwi and M. Grätzel, *Nature*, 1987, **327**, 506-508.

64 G. Kim, S. Lee, J. Y. Shin, G. Corre, J. T. S. Irvine, J. M. Vohs and R. J. Gorte, *Electrochem. Solid-State Lett.*, 2009, **12**, B48-B52.

65 H. Lv, H.-y. Tu, B.-y. Zhao, Y.-j. Wu and K.-a. Hu, *Solid State Ionics*, 2007, **177**, 3467-3472.

66 B. Huang, S. R. Wang, R. Z. Liu and T. L. Wen, *J. Power Sources*, 2007, **167**, 288-294.

67 K. Xie, Y. Q. Zhang, G. Y. Meng and J. T. S. Irvine, *J. Mater. Chem.*, 2011, **21**, 195-198.

68 G. Schiller, A. Ansar, M. Lang and O. Patz, *J. Appl. Electrochem.*, 2009, **39**, 293-301.

69 S. Wang , GQ (Max) Lu, *Ener. & Fuels*, 1996, 10, 896-904.

70 A. P. E. York, J. B. Claridge, A. J. Brungs, S. C. Tsang and M. L. H. Green, *Chem. Commun.*, 1997, 39.

Captions

Fig. 1 XRD Rietveld refinement patterns of the oxidized (a1) LSTO and (b1) iron-loaded LSTO; the reduced (a2) LSTO and (b2) iron-loaded LSTO.

Fig. 2 The TEM graph of the (a) oxidized LSTO; (b) reduced LSTO.

Fig. 3 XPS results for Ti (a1) in the oxidized LSTO， Ti (a2) in the reduced LSTO； Ti (b1) and Fe (c1) in the oxidized iron-loaded LSTO; Ti (b2) and Fe (c2) in the reduced iron-loaded LSTO.

Fig. 4 Mixed conductivities of the (a) LSTO electrode and (b) iron-loaded LSTO electrode in redox-cycling atmospheres.

Fig. 5 AC impedance spectroscopy of YSZ-supported symmetrical cells based on (a1) (a2) LSTO electrodes and (b1) (b2) iron-loaded LSTO at different hydrogen partial pressure at 800 °C.

Fig. 6 AC impedance spectroscopy of YSZ-supported symmetrical cells based on (a1) (a2) LSTO electrodes and (b1) (b2) iron-loaded LSTO at different methane partial pressure at 800 °C.

Fig. 7 SEM picture of the (a) LSTO-SDC and (b) iron-loaded LSTO-SDC electrodes on the YSZ electrolyte.

Fig. 8 (a) The I-V curves of two electrolyzers at 800 ^{o}C in 20%CO_2/20%CH_4/60%Ar; (b) the performances of biogas dry reforming for electrolyzer at 800 ^{o}C in 20%CO_2/20%CH_4/60%Ar.

Fig. 9 The AC impendence of the electrolysis cells based on LSTO (a1, a2) and iron-loaded LSTO (b1, b2) with the flow of 20%CH_4/20%CO_2/60%Ar at 800 ^{o}C.

Fig. 10 The conversion of CO_2 and CH_4 : (a) based on LSTO and (b2) based on iron-loaded LSTO in the flow of 20%CH_4/20%CO_2/60%Ar at 800 ^{o}C.

Fig. 11 (a) The production of H_2; (b) The production of CO with LSTO and iron-loaded LSTO in the flow of 20%CH_4/20%CO_2/60%Ar at 800 ^{o}C.

Fig. 1

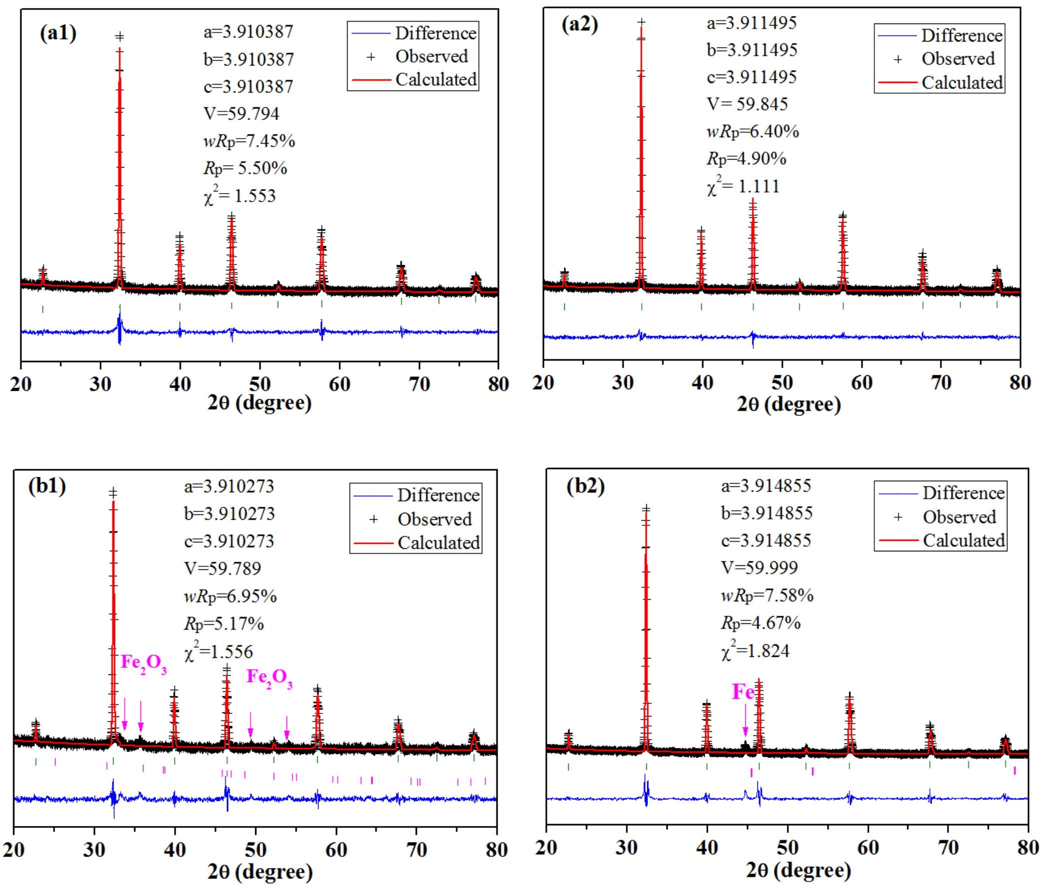
(a1)
a=3.910387
b=3.910387
c=3.910387
V=59.794
wRp=7.45%
Rp= 5.50%
χ2= 1.553
Difference
Observed
Calculated
2θ (degree)
(a2)
a=3.911495
b=3.911495
c=3.911495
V= 59.845
wRp=6.40%
Rp=4.90%
χ2= 1.111
(b1)
a=3.910273
b=3.910273
c=3.910273
V=59.789
wRp=6.95%
Rp=5.17%
χ2=1.556
Fe2O3
Fe2O3
(b2)
a=3.914855
b=3.914855
c=3.914855
V=59.999
wRp=7.58%
Rp=4.67%
χ2=1.824
Fe
20
30
40
50
60
70
80

Fig. 2

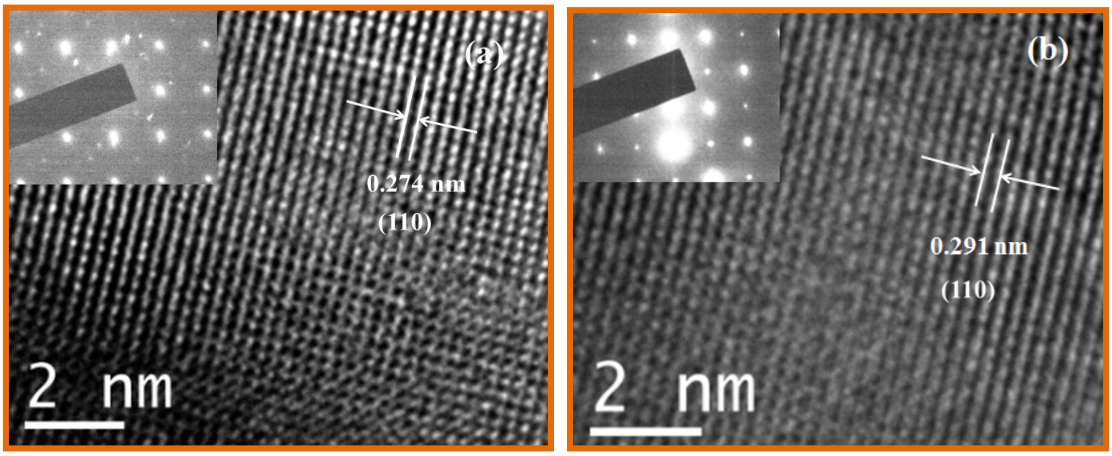

Fig. 3

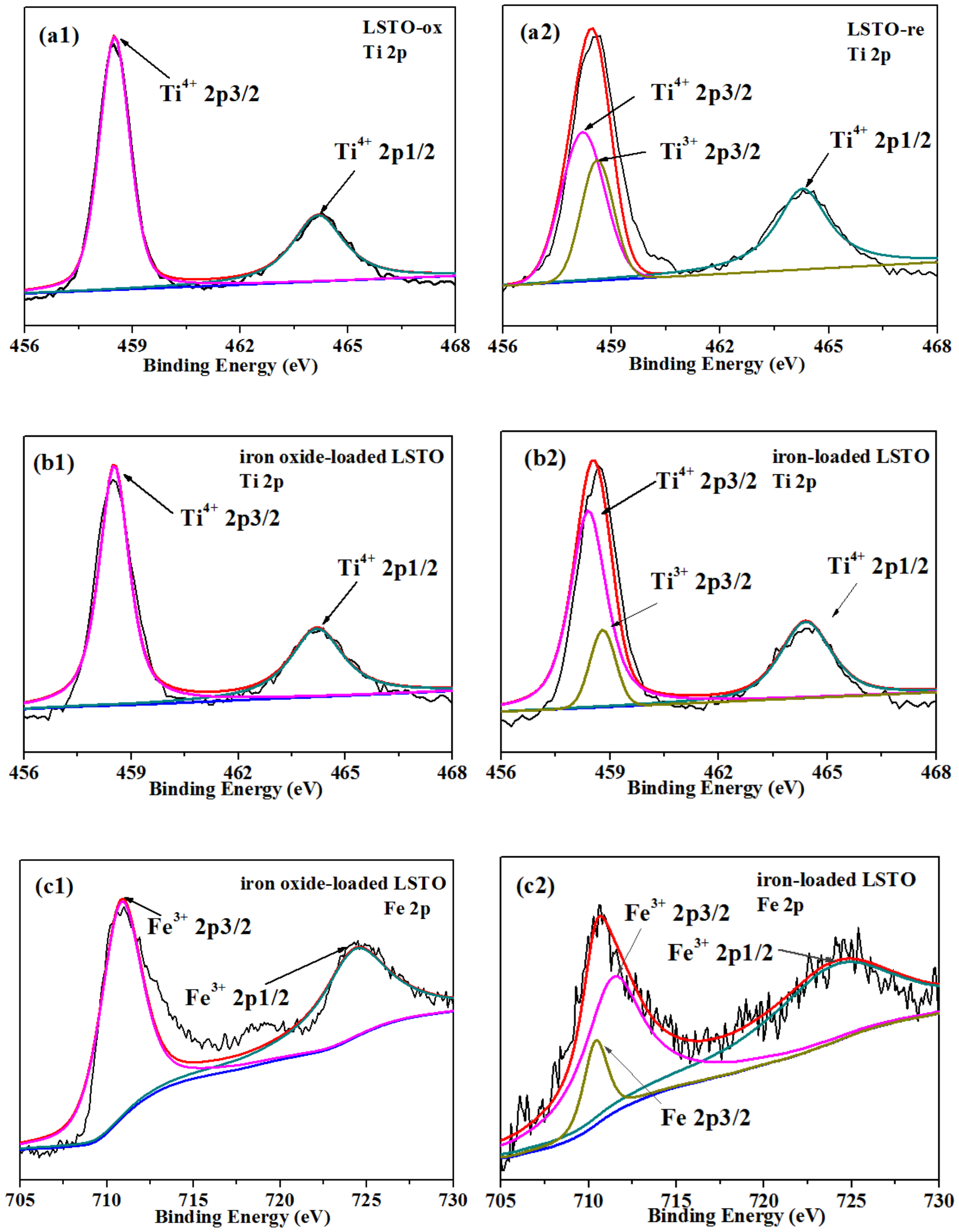
(a1)
LSTO-ox
Ti 2p
Ti^{4+} 2p3/2
Ti^{4+} 2p1/2
456
459
462
465
468
Binding Energy (eV)
(a2)
LSTO-re
Ti 2p
Ti^{4+} 2p3/2
Ti^{3+} 2p3/2
Ti^{4+} 2p1/2
456
459
462
465
468
Binding Energy (eV)
(b1)
iron oxide-loaded LSTO
Ti 2p
Ti^{4+} 2p3/2
Ti^{4+} 2p1/2
456
459
462
465
468
Binding Energy (eV)
(b2)
iron-loaded LSTO
Ti 2p
Ti^{4+} 2p3/2
Ti^{3+} 2p3/2
Ti^{4+} 2p1/2
456
459
462
465
468
Binding Energy (eV)
(c1)
iron oxide-loaded LSTO
Fe 2p
Fe^{3+} 2p3/2
Fe^{3+} 2p1/2
705
710
715
720
725
730
Binding Energy (eV)
(c2)
iron-loaded LSTO
Fe 2p
Fe^{3+} 2p3/2
Fe^{3+} 2p1/2
Fe 2p3/2
705
710
715
720
725
730
Binding Energy (eV)

Fig. 4

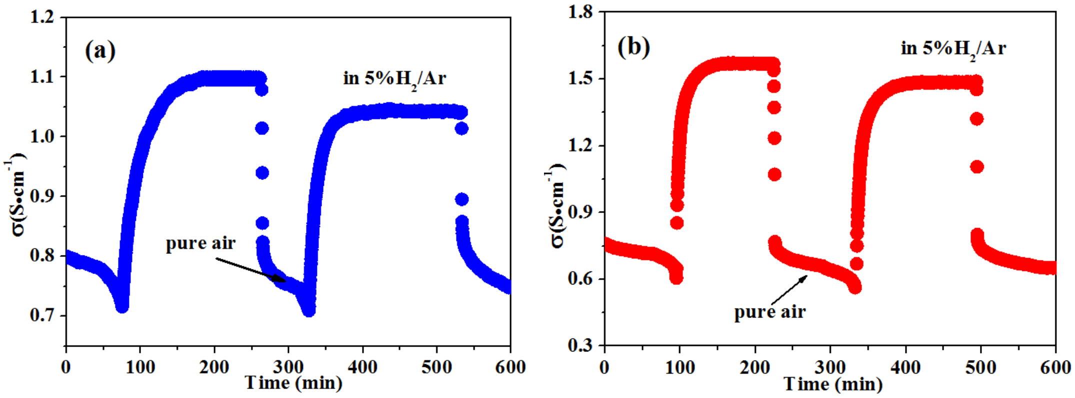
(a)
in 5%H$_2$/Ar
pure air
σ(S•cm^{-1})
Time (min)
1.2
1.1
1.0
0.9
0.8
0.7
0
100
200
300
400
500
600
(b)
in 5%H$_2$/Ar
pure air
σ(S•cm^{-1})
Time (min)
1.8
1.5
1.2
0.9
0.6
0.3

Fig. 5

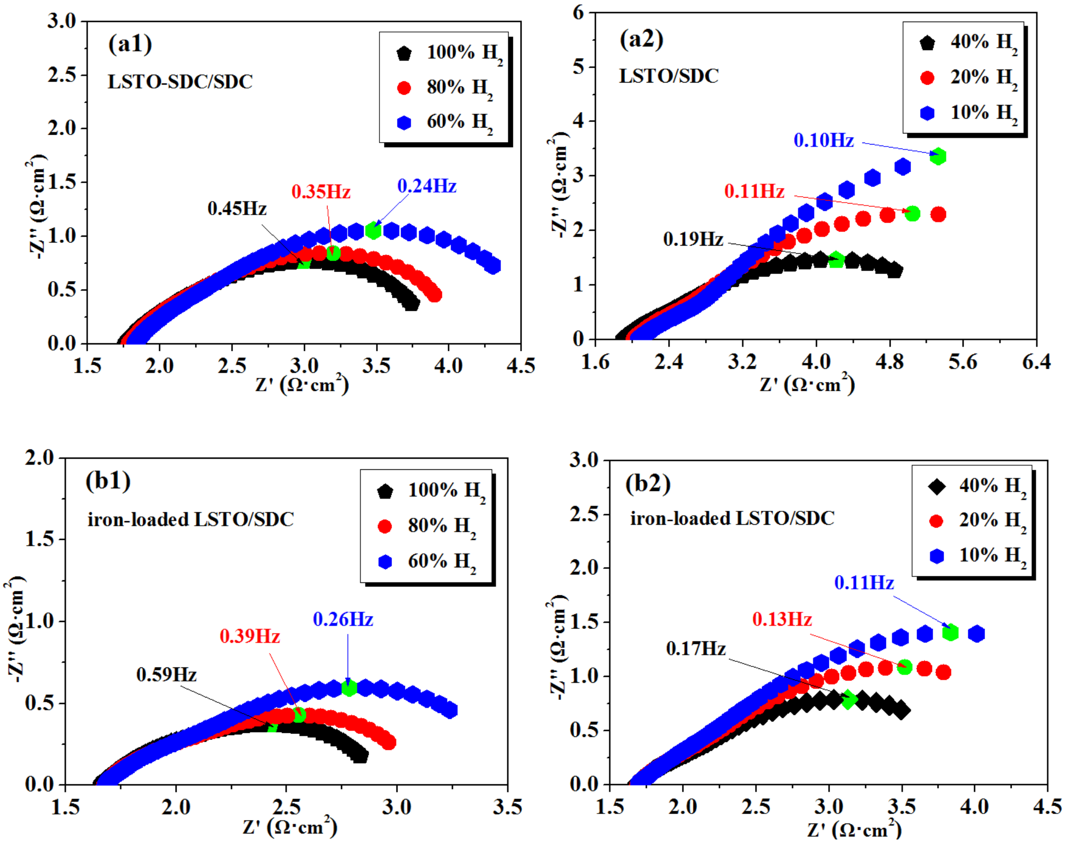
(a1)
LSTO-SDC/SDC
100% H_2
80% H_2
60% H_2
0.45Hz
0.35Hz
0.24Hz
-Z'' (Ω·cm^2)
Z' (Ω·cm^2)
0.0
0.5
1.0
1.5
2.0
2.5
3.0
1.5
2.0
2.5
3.0
3.5
4.0
4.5
(a2)
LSTO/SDC
40% H_2
20% H_2
10% H_2
0.10Hz
0.11Hz
0.19Hz
-Z'' (Ω·cm^2)
Z' (Ω·cm^2)
0
1
2
3
4
5
6
1.6
2.4
3.2
4.0
4.8
5.6
6.4
(b1)
iron-loaded LSTO/SDC
100% H_2
80% H_2
60% H_2
0.26Hz
0.39Hz
0.59Hz
-Z'' (Ω·cm^2)
Z' (Ω·cm^2)
0.0
0.5
1.0
1.5
2.0
1.5
2.0
2.5
3.0
3.5
(b2)
iron-loaded LSTO/SDC
40% H_2
20% H_2
10% H_2
0.11Hz
0.13Hz
0.17Hz
-Z'' (Ω·cm^2)
Z' (Ω·cm^2)
0.0
0.5
1.0
1.5
2.0
2.5
3.0
1.5
2.0
2.5
3.0
3.5
4.0
4.5

Fig. 6

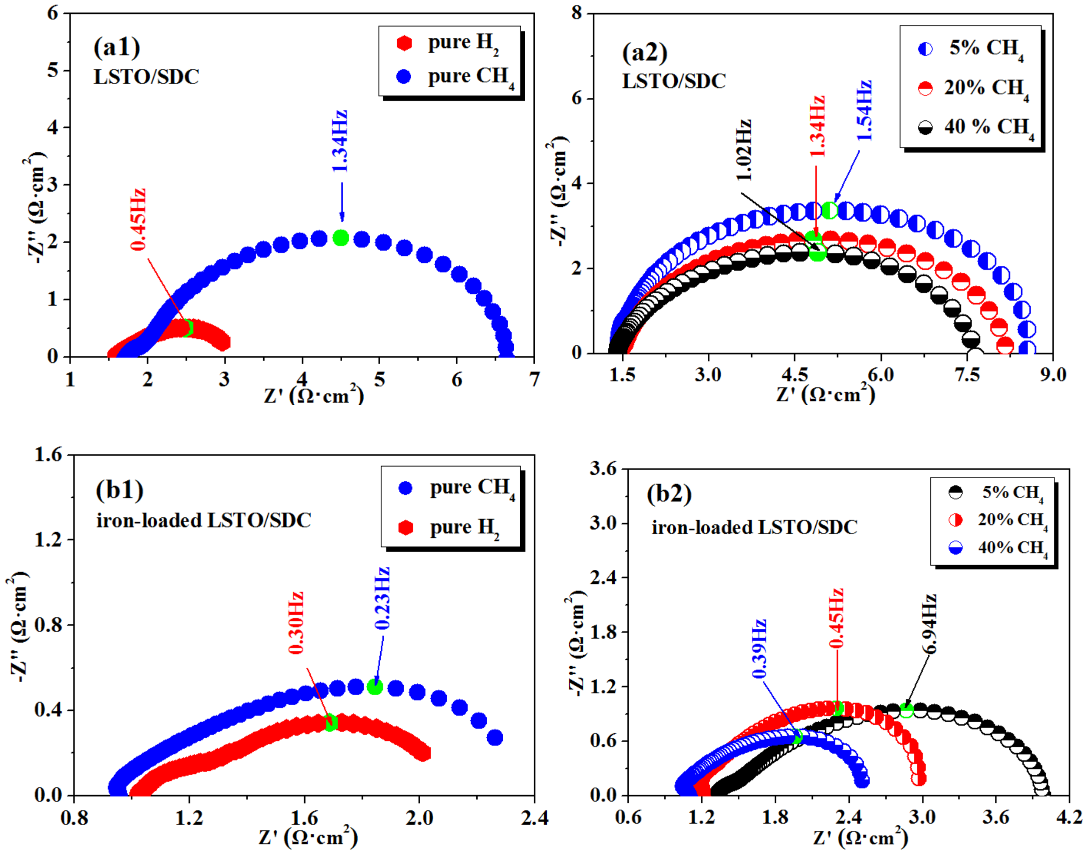
(a1)
LSTO/SDC
pure H$_2$
pure CH$_4$
0.45Hz
1.34Hz
-Z'' (Ω·cm^2)
Z' (Ω·cm^2)
(a2)
LSTO/SDC
5% CH$_4$
20% CH$_4$
40 % CH$_4$
1.02Hz
1.34Hz
1.54Hz
(b1)
iron-loaded LSTO/SDC
pure CH$_4$
pure H$_2$
0.30Hz
0.23Hz
(b2)
iron-loaded LSTO/SDC
5% CH$_4$
20% CH$_4$
40% CH$_4$
0.39Hz
0.45Hz
6.94Hz

Fig. 7

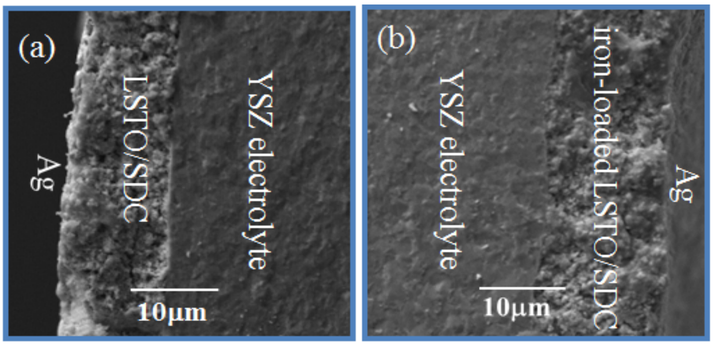
(a)
Ag
LSTO/SDC
YSZ electrolyte
10µm
(b)
YSZ electrolyte
iron-loaded LSTO/SDC
Ag
10µm

Fig. 8

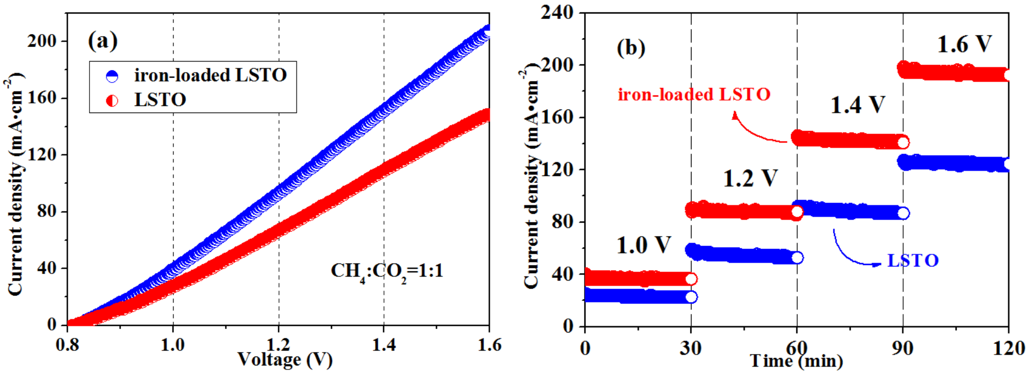
(a)
iron-loaded LSTO
LSTO
CH$_4$:CO$_2$=1:1
Current density (mA·cm^{-2})
Voltage (V)
0
40
80
120
160
200
0.8
1.0
1.2
1.4
1.6
(b)
iron-loaded LSTO
LSTO
1.0 V
1.2 V
1.4 V
1.6 V
Current density (mA•cm^{-2})
Time (min)
0
40
80
120
160
200
240
0
30
60
90
120

Fig. 9

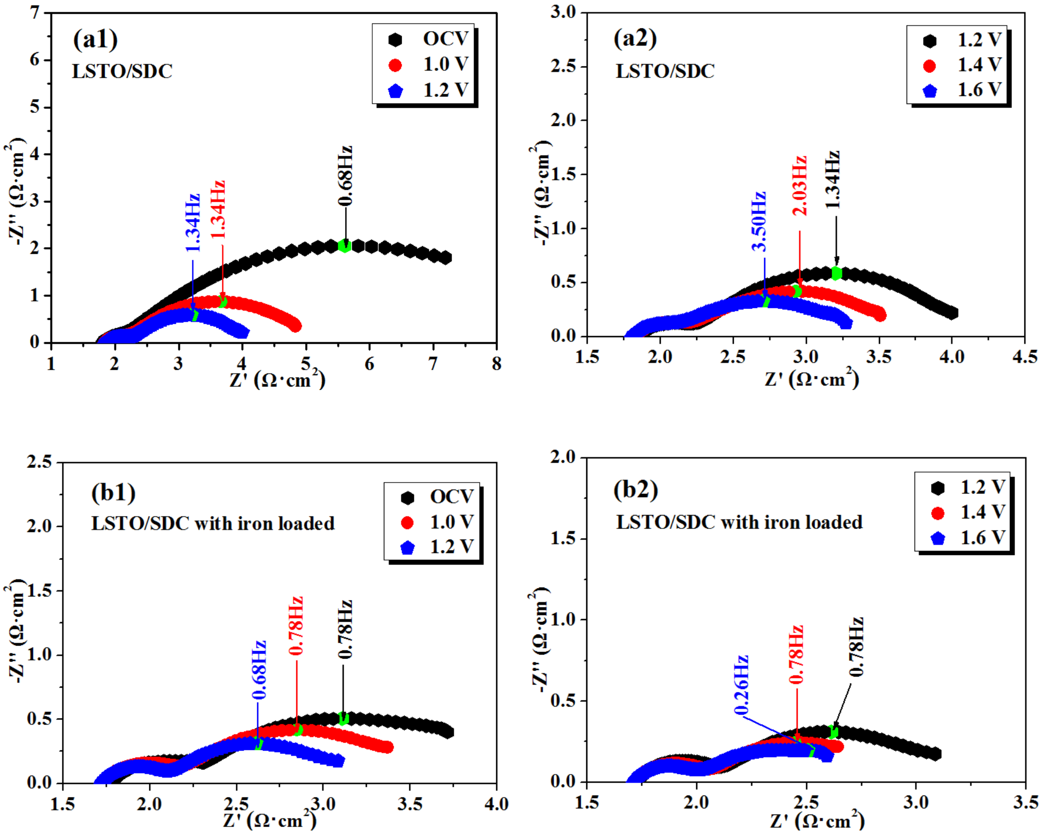
(a1)
LSTO/SDC
● OCV
● 1.0 V
⬟ 1.2 V
1.34Hz
1.34Hz
0.68Hz
-Z'' (Ω·cm^2)
Z' (Ω·cm^2)
(a2)
LSTO/SDC
● 1.2 V
● 1.4 V
⬟ 1.6 V
3.50Hz
2.03Hz
1.34Hz
(b1)
LSTO/SDC with iron loaded
● OCV
● 1.0 V
⬟ 1.2 V
0.68Hz
0.78Hz
0.78Hz
(b2)
LSTO/SDC with iron loaded
● 1.2 V
● 1.4 V
⬟ 1.6 V
0.26Hz
0.78Hz
0.78Hz

Fig. 10

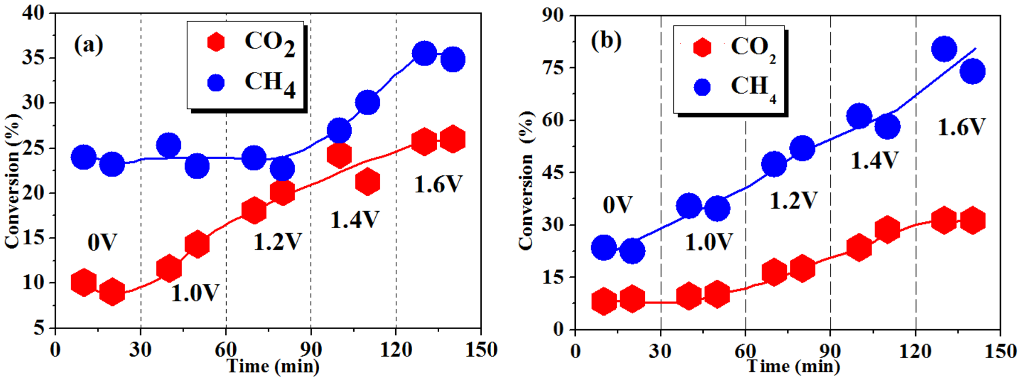
(a)
CO$_2$
CH$_4$
Conversion (%)
Time (min)
0V
1.0V
1.2V
1.4V
1.6V
40
35
30
25
20
15
10
5
0
30
60
90
120
150
(b)
CO$_2$
CH$_4$
Conversion (%)
Time (min)
0V
1.0V
1.2V
1.4V
1.6V
90
75
60
45
30
15
0
0
30
60
90
120
150

Fig. 11

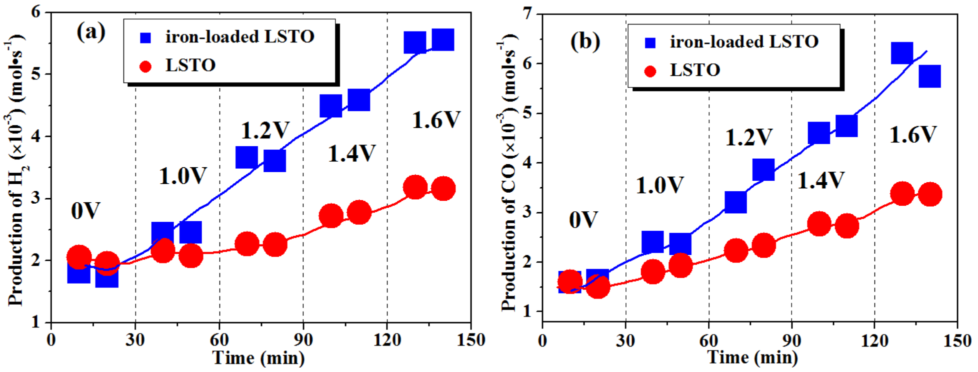
(a)
Production of H_2 ($\times10^{-3}$) (mol•s^{-1})
Time (min)
iron-loaded LSTO
LSTO
0V
1.0V
1.2V
1.4V
1.6V
1
2
3
4
5
6
0
30
60
90
120
150
(b)
Production of CO ($\times10^{-3}$) (mol•s^{-1})
Time (min)
iron-loaded LSTO
LSTO
0V
1.0V
1.2V
1.4V
1.6V
1
2
3
4
5
6
7
0
30
60
90
120
150